AGU PUBLICATIONS

JGR

Journal of Geophysical Research: Oceans

RESEARCH ARTICLE

10.1002/2016JC011983

Key Points:
- The variability of chlorophyll *a* concentration in the open South China Sea was observed by Bio-Argo floats
- In a year round, chlorophyll *a* concentration displayed a different variability in the northern and central parts of the SCS basin
- The physical drivers of chlorophyll variability in the open South China Sea were examined

Correspondence to:
W.-Z. Zhang,
zwenzhou@xmu.edu.cn

Citation:
Zhang, W.-Z., H. Wang, F. Chai, and G. Qiu (2016), Physical drivers of chlorophyll variability in the open South China Sea, *J. Geophys. Res. Oceans*, *121*, 7123–7140, doi:10.1002/2016JC011983.

Received 23 MAY 2016
Accepted 7 SEP 2016
Accepted article online 10 SEP 2016
Published online 28 SEP 2016

Physical drivers of chlorophyll variability in the open South China Sea

Wen-Zhou Zhang[1,2,3], Haili Wang[1], Fei Chai[4,5], and Guoqiang Qiu[1]

[1]State Key Laboratory of Marine Environmental Science, Xiamen University, Xiamen, China, [2]Fujian Provincial Key Laboratory for Coastal Ecology and Environmental Studies, Xiamen University, Xiamen, China, [3]Key Laboratory of Underwater Acoustic Communication and Marine Information Technology, Xiamen University, Ministry of Education, Xiamen, China, [4]School of Marine Sciences, University of Maine, Orono, Maine, USA, [5]State Key Laboratory of Satellite Ocean Environment Dynamics, Second Institute of Oceanography, SOA, Hangzhou, China

Abstract The variability of chlorophyll *a* concentration (Chl *a*) in the open South China Sea (SCS) was examined using observations from two Bio-Argo floats. During the period of September 2014 to August 2015, there was a permanent subsurface Chl *a* maximum (SCM) in the depth range of 48 to 96 m in the central basin of the SCS. In the northern basin, the SCM disappeared in winter, replaced by enhanced surface layer phytoplankton with high Chl *a*. The values of the SCM were influenced by the vertical displacement of isotherms. Strong wind forcing and surface cooling were the main physical drivers of high surface Chl *a* in winter. In the north, stronger wind than in the center, lower sea surface temperature (SST) than in the center, and Kuroshio water intrusion were more favorable for the upward transport of nutrient-rich deep water. A large amount of nitrate could be advected from the Taiwan Strait and shallow continental shelf to the northern basin in winter. A combination of strong wind mixing, surface cooling, Kuroshio water intrusion, and horizontal advection caused the winter surface phytoplankton bloom in the north.

1. Introduction

The South China Sea (SCS) is the largest marginal sea of the western North Pacific Ocean, extending from 3°S to 23°N and from 99°E to 121°E. It is a semiclosed deep sea with a complex topography, including two wide shallow shelves in the northern and southern parts and a large deep basin in between. The deep basin has a maximum depth of approximately 4700 m [*Chu and Li*, 2000]. It interacts with the East China Sea, the Pacific Ocean, and the Sulu Sea via the Taiwan Strait, the Luzon Strait, and the Mindoro Strait, respectively (Figure 1a).

The East Asian Monsoon System controls or regulates circulations, mixed layer depth (MLD), and thermocline in the upper SCS [*Chu et al.*, 1999; *Liu et al.*, 2000; *Qu et al.*, 2007]. Strong northeasterly winds prevail in winter while southwesterly winds dominate in summer. The transition between them takes place in May and September. As a result, overall basin-scale circulation is cyclonic in winter but anticyclonic in summer [*Chu et al.*, 1999; *Hu et al.*, 2000; *Zhang et al.*, 2015b]. In the northern SCS, surface currents originating from the Taiwan Strait and the Luzon Strait flow southwestward in winter, instead of northeastward currents in summer [*Chu et al.*, 1999]. The southwestward current from the shallow Taiwan Strait has low temperature and high nutrients [*Chen et al.*, 2013]. By contrast, the current branching from the Kuroshio through the Luzon Strait has higher temperature and salinity but lower nutrients than the SCS water [*Chen et al.*, 2010].

The change of the MLD in the SCS is mainly related to wind stress, net surface heat flux, and net freshwater flux [*Qu et al.*, 2007; *Fan et al.*, 2010; *Duan et al.*, 2012]. Among these three factors, wind stress and net surface heat flux are more important [*Fan et al.*, 2010; *Duan et al.*, 2012]. The net surface heat flux is the sum of sensible heat flux, latent heat flux, net shortwave radiation, and net longwave radiation [*Shinoda et al.*, 1998; *Zhang et al.*, 2012]. In the surface heat budget, insolation, and latent heat flux are the dominant components [*Shinoda et al.*, 1998]. Using historic hydrographic data, *Duan et al.* [2012] showed that the mixed layer in the SCS is deeper in winter than in summer. They found that net surface heat flux is the main driver of the MLD in winter but wind stress is dominant over the net surface heat flux in summer. Net surface heat flux drives the seasonal variation of the sea surface temperature (SST) in the SCS [*Qu*, 2001]. *Qu* [2001]

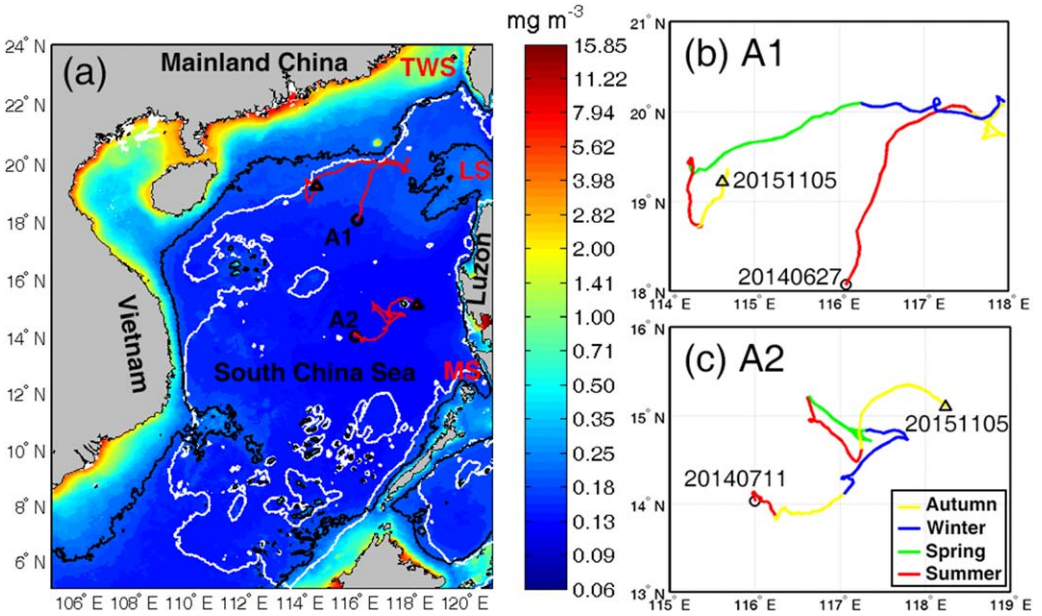

Figure 1. Geographic map and Bio-Argo floats' trajectories: (a) geographic map with the trajectories (red curves) of Bio-Argo floats A1 and A2; (b) trajectory of A1; (c) trajectory of A2. In (a), the colors show the climatological Chl *a* averaged from July 2002 to June 2015, and the thick black contour denotes 0.2 mg m^{-3}; the white curve is the isobath of 1000 m. TWS, LS, and MS are the abbreviations of the Taiwan Strait, the Luzon Strait, and the Mindoro Strait, respectively. Different colored segments in Figures 1b and 1c show the trajectories of floats during different seasons. The black solid circle and triangle denote the start and end points of a float's trajectory, respectively.

showed that there is a negative correlation between the MLD and the SST. In winter, negative net surface heat flux (sea surface losing heat) decreases the SST (surface cooling), which makes the surface layer water unstable and together with wind stirring produces a deep mixed layer; in summer, positive net surface heat flux (sea surface gaining heat) increases the SST (surface warming), which makes the surface layer water stable and results in a shallow mixed layer [*Duan et al*., 2012]. *Qu et al*. [2007] noted that wind stirring and surface cooling primarily determine the basin-wide variation of isothermal depth (a good proxy of the MLD) in the SCS. The thermocline in the open SCS is weaker and thinner in winter than in summer, especially in the northern basin [*Liu et al*., 2000, 2001; *Hao et al*., 2012]. Additionally, both the MLD and the thermocline in the SCS may be influenced by local eddies and the intrusion of Kuroshio water through the Luzon Strait [*Chu et al*., 1999; *Liu et al*., 2000, 2001; *Qu et al*., 2007]. Cyclonic eddy tends to uplift the thermocline while anticyclonic eddy tends to depress the thermocline [*Liu et al*., 2001]. *Liu et al*. [2000] attributed a thicker mixing layer in winter, than that in summer, to Kuroshio water in the northeastern SCS. *Qu et al*. [2007] argued that Kuroshio intrusion potentially has an important influence on the isothermal depth.

Aside from shallow coastal areas with high primary productivity, the SCS is oligotrophic [*Shen et al*., 2008; *Liu et al*., 2013]. With the advent of abundant satellite remote sensing ocean color data, seasonally high chlorophyll *a* concentration (Chl *a*) has been found in the wind-driven upwelling or jet areas northeast of Luzon Island and southeast of Vietnam [*Tang et al*., 1999; *Liu et al*., 2002]. Although Chl *a* is not equivalent or linearly proportional to phytoplankton concentration [*Cullen*, 2015], it has been taken as one proxy or indicator of phytoplankton biomass because of its indispensable role in the photosynthesis of phytoplankton [e.g., *Tang et al*., 2004, 2014]. Some synoptic scale phytoplankton blooms caused by typhoons were also observed via surface Chl *a* variation in the open SCS [*Lin et al*., 2003; *Shang et al*., 2008]. Because of strong signals identified easily and great contributions to primary production, many studies have focused on these local or episodic events. By contrast, less attention was paid to the variability of Chl *a* in normal conditions at the annual timescale. The Chl *a* in this respect provides an essential ecological background for the open SCS.

Satellite remote sensing data show that surface Chl *a* in the SCS exhibits a pronounced seasonal variation [*Shen et al*., 2008; *Palacz et al*., 2011; *Liu et al*., 2013; *Tang et al*., 2014]. Based on monthly mean SeaWiFS data during the period of September 1997 to December 2006, *Shen et al*. [2008] demonstrated that in the

northern SCS Chl *a* reached its maximum (larger than 0.3 mg m^{-3}) in winter and minimum (0.1–0.15 mg m^{-3}) in summer. In the sea area of 17°N–19°N and 115°E–117°E, the satellite data merged from SeaWiFS (1997–2007) to MODIS (2003–2011) indicated that monthly mean Chl *a* was in the range of 0.04–0.47 mg m^{-3} and large peaks occurred in winter [*Liu et al*., 2013]. In winter, extreme Chl *a* usually appears northwest of Luzon Island where a daily maximum may exceed 3.0 mg m^{-3} [*Shen et al*., 2008]. *Tang et al*. [1999] also reported that a larger bloom with an area of 20,000 km^2 happened in this region in December 1979 and the pigment concentration in the bloom center was approximately 2.5 mg m^{-3}. A high surface Chl *a* of 2.17 mg m^{-3} was observed at a site (17°N, 118°E) west of Luzon Island by a field survey during the period from September to November 1980 [*Tang et al*., 1999].

In the oligotrophic open SCS, phytoplankton growth is limited by nutrients [*Tang et al*., 2004; *Chen*, 2005]. Physical processes (e.g., wind mixing and upwelling) play an important and indispensable role in supplying nutrients for the phytoplankton growth which changes Chl *a* in the SCS [*Wang et al*., 2010; *Liu et al*., 2013; *Tang et al*., 2014]. Previous studies demonstrated that the Chl *a* variability in the surface layer of the SCS is closely related to wind forcing and SST cooling [e.g., *Liu et al*., 2013; *Liu and Chen*, 2014]. In coastal sea areas near middle Vietnam coast and northwest of Luzon Island, strong wind stress and wind stress curl can produce upwelling by wind-driven offshore Ekman transport and Ekman pumping, respectively, which drives nutrient-rich water upward and then triggers or fuels phytoplankton bloom [*Tang et al*., 2004; *Wang et al*., 2010; *Yang et al*., 2012]. Strong wind stirring deepens the MLD and entrains nutrients to the surface layer [*Wang et al*., 2010; *Duan et al*., 2012]. Chl *a* correlates significantly with wind speed in the open SCS, and its correlation with the SST is significant in the northern SCS [*Shen et al*., 2008; *Liu et al*., 2013; *Tang et al*., 2014]. Surface cooling weakens the stratification of water column and enhances vertical convection, which brings more nutrients upward [*Duan et al*., 2012; *Tang et al*., 2014]. By contrast, surface warming strengthens the stratification, potentially preventing upward transport of nutrients [*Duan et al*., 2012; *Liu and Chen*, 2014]. Compared with wind speed and SST, the correlation between surface Chl *a* and wind stress curl is very weak in the open SCS [*Tang et al*., 2014]. A deep thermocline is unfavorable for the increase of surface Chl *a* because the deep thermocline makes wind effect on nutrient transport less efficient [*Liu et al*., 2013].

In the vertical structure of Chl *a*, a layer with elevated Chl *a* may appear in the subsurface, so-called subsurface Chl *a* maximum (SCM) or deep Chl *a* maximum [*Cullen*, 2015]. The SCM is a nearly ubiquitous feature in stably stratified waters [*Liu et al*., 2002; *Cullen*, 2015]. The depth of the SCM is consistent with the top of the nitracline where phytoplankton growth is enhanced by the optimal combination of nutrient flux and irradiance [*Cullen*, 2015]. Nutrients above this depth are depleted, resulting in a lower surface layer Chl *a*; available light below this depth is inadequate, limiting the growth of phytoplankton [*Mignot et al*., 2011]. In the layer of the SCM, the ratio of Chl *a* to phytoplankton carbon is higher than that in the nutrient-depleted surface layer because of photoacclimation of phytoplankton to lower light [*Fennel and Boss*, 2003]. At the top of nutricline, the sinking of phytoplankton slows down and may accentuate the SCM [*Steele and Yentsch*, 1960; *Cullen*, 2015]. This effect is not important in oligotrophic waters [*Bienfang et al*., 1983; *Fennel and Boss*, 2003]. The swimming behavior of motile phytoplankton and the buoyancy regulation of nonmotile phytoplankton can also affect the vertical structure of Chl *a* [*Stacey et al*., 2007; *Durham and Stocker*, 2012]. The above interacting biological and biogeochemical processes form and maintain the SCM, and all these processes are influenced by physical processes or hydrodynamics [*Cullen*, 2015].

In the SCS, the SCM was sporadically captured by in situ observations [e.g., *Chen et al*., 2006; *Liu et al*., 2002]. *Liu et al*. [2002] observed a deeper SCM at 75 m in September 1998 and a shallower at 40–50 at the same site (18.0°N, 118.5°E) in January 1999 in the northern SCS. They also observed a strong SCM (0.47 mg m^{-3}) at 60 m, three times the surface Chl *a* (0.15 mg m^{-3}), in March 2000 at another site (18.0°N, 115.5°E). Based on the bimonthly shipboard observations along a section from Kaohsung to a station (19.0°N, 118.5°E) during the period of September 1998 to July 1999 except for November 1998, *Chen et al*. [2006] asserted that the SCM was higher in winter and lower in other seasons. A three-dimensional physical-biogeochemical coupled numerical model predicted the SCM in the SCS, although its depth was shallower than the observed [*Liu et al*., 2002]. A one-dimensional physical-biochemical coupled model showed that wind speed can change the intensity of the SCM in winter and summer, but has a minor effect on its depth [*Gong et al*., 2014].

Satellite remote sensing data have played an important role in studies on the variability of surface Chl *a*, like those mentioned previously. However, they become helpless in examining the vertical structure of Chl

a since they are limited to the surface layer. In situ observations by survey ships were sparse in both time and space, especially in remote open oceans [*Mignot et al*., 2014]. In addition to biological and biogeochemical processes, Chl *a* variability is influenced by physical processes [*Cullen*, 2015]. The variability of Chl *a*, particularly vertical structure, and its driving physical processes in the open SCS remains unclear due to lack of in situ observations. The SCS is a unique semiclosed marginal sea with a large deep basin under the influence of the East Asian Monsoon System, determining its distinctive biogeochemical and hydrodynamic environments [*Wyrtki*, 1961; *Liu et al*., 2002]. The aim of this work is to obtain a relatively complete picture of the spatial and temporal variability of Chl *a* during a whole year and examine its physical drivers in the open SCS using two Bio-Argo floats' data, which is the first attempt to apply Bio-Argo floats in examining Chl *a* variability in the SCS. Bio-Argo floats have invaluable advantages in observing biogeochemical properties and their dynamics with a fine sampling resolution over long time periods in remote open oceans [*Mignot et al*., 2014]. The observations of Bio-Argo floats showed that in a year round, Chl *a* displayed a different variability in the northern and central parts of the SCS basin. The vertical displacement of isotherms affected the values of the SCM. Strong wind forcing and surface cooling were the main physical drivers of upward nutrient supply and then high surface Chl *a* in winter. The combination of stronger wind mixing, greater surface cooling, Kuroshio water intrusion, and horizontal advection caused a winter bloom in the northern basin rather than in the central basin. The results presented here will be valuable to understand the variability of Chl *a* and its relationship with physical processes in the deep region of a marginal sea like the SCS.

2. Data and Method

2.1. Bio-Argo Observations

Recently, Bio-Argo floats with biogeochemical sensors have been successfully used to monitor ocean environment variability [e.g., *Xing et al*., 2011; *Green et al*., 2014; *Mignot et al*., 2014]. Two Bio-Argo floats (Navis Autonomous Profiling Floats) numbered 0347 and 0348 (identification numbers assigned by the manufacturer, referred to as A1 and A2, respectively, in this paper) were deployed in the northern and central parts of the open SCS basin on 27 June and 11 July 2014, respectively. Their traveling paths are shown in Figure 1. Each of them was equipped with an SBE 41CP CTD, an SBE 63 Optical Dissolved Oxygen sensor, and a WET Labs ECO-MCOMS fluorometer. These two floats were provided by the manufacturer at the same time, supposed to be based on the same technology and agree with each other. They were set to obtain one vertical profile every 3 days during most of the deployment period and sometimes adjusted to profile once per day for a few short periods. The vertical observation interval was approximately 2 m from approximately 4 to 1000 m depth and 50 m below 1000 m depth.

The two Bio-Argo floats measured physical, biogeochemical, and optical parameters including salinity, temperature, pressure (depth), Chl *a*, Colored Dissolved Organic Matter (CDOM), dissolved oxygen, volume scattering coefficient at 700 nm and 150°, water and particle backscattering coefficients at 700 nm. The Chl *a* is not a directly measured parameter. It was derived from fluorescence (measured by the ECO-MCOMS fluorometer) based on a linear relationship between Chl *a* and fluorescence as well as a prescribed scale factor, which was determined beforehand by the manufacturer. Since the relationship and scale factor are based upon the experimental results using a monoculture of phytoplankton, there is inevitably some uncertainty in the derived values of Chl *a*. In reality, the scale factor between in vivo fluorescence and Chl *a* depends on species composition, nutrient availability, and ambient light [*Fennel and Boss*, 2003; *Xing et al*., 2011]. Another significant phenomenon affecting the accurate retrieval of Chl *a* is nonphotochemical fluorescence quenching in daytime, the so-called daytime fluorescence quenching [*Sackmann et al*., 2008; *Xing et al*., 2011]. The extent of quenching is closely related to incoming solar radiation: greater in summer and less in winter because of the difference in light level and daytime length [*Sackmann et al*., 2008]. *Sackmann et al*. [2008] found that the quenching is most prominent near the surface and reduces with depth; near-surface daytime fluorescence can decrease by as much as 80% in summer. Nonphotochemical fluorescence quenching tends to disappear at night [*Chekalyuk et al*., 2000; *Huot and Babin*, 2011].

The data during a 1 year period from September 2014 to August 2015 was used in this study. The two floats profiled almost synchronously (i.e., in the same days) from 18 September 2014 until the end of the period in August 2015. Prior to 18 September 2014, there was a 1 day shift between their profiles. Only three profiles

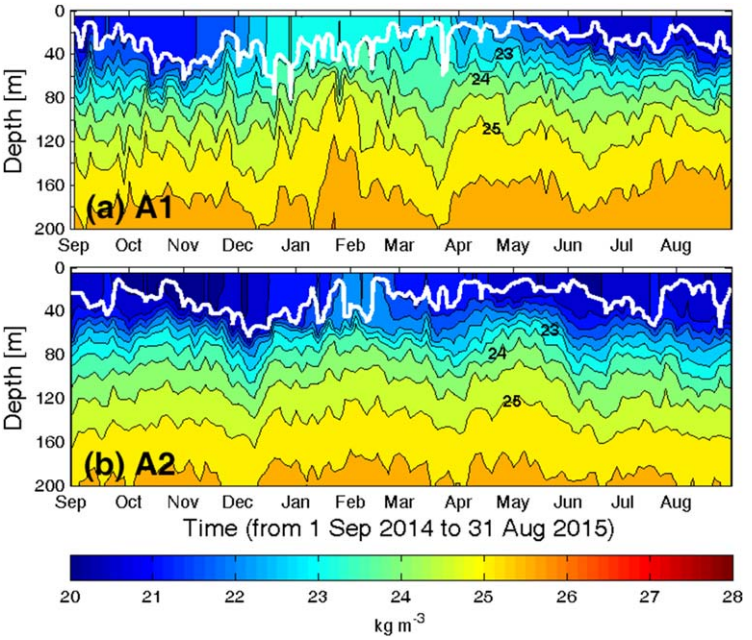

Figure 2. Time series of potential density (minus 1000 kg m^{-3}) derived from observations of Bio-Argo floats (a) A1 and (b) A2. The white curve denotes the MLD. The interval of contours is 0.5 kg m^{-3}.

were collected by A1 in the afternoon during early September 2014, and the other profiles were obtained at night, which avoided the influence of high irradiance in the daytime due to daytime fluorescence quenching.

Based on pressure, salinity, and temperature observations, corresponding absolute salinity and conservative temperature were calculated via Gibbs Seawater oceanographic toolbox (version 3.0) of the International Thermodynamic Equation of Seawater-2010 (TEOS-10). Then, potential density (with respect to reference pressure of 0 dbar) and buoyancy (Brunt-Väisälä) frequency square (N^2) were derived from the absolute salinity and conservative temperature. The MLD (see Figure 2) was estimated according to a threshold of 0.06 kg m^{-3}, the difference in potential density between 10 m depth and the base of the mixed layer [*Zhang et al*., 2015a].

2.2. Comparison Between Bio-Argo Chl *a* and Remote Sensing Data

We compared Bio-Argo-observed Chl *a* at 5 m depth with daily remote sensing derived surface Chl *a* obtained by Moderate Resolution Imaging Spectroradiometer (MODIS)/Aqua instruments [*Hu et al*., 2012]. This remote sensing Chl *a* data set has a resolution of 4 km. For each Bio-Argo profile, the remote sensing Chl *a* data recorded in the same day were averaged in a 0.4° × 0.4° box centered by the profile, resulting in a sample pair. Because remote sensing Chl *a* data were missing in most days due to clouds or sun glitter, the number of available pairs was much smaller than that of Bio-Argo profiles. Seen from available pairs, the Bio-Argo-observed Chl *a* data are in agreement with remote sensing data (Figure 3) despite a slight difference in observation depth. The mean absolute error is 0.043 mg m^{-3} (35 pairs) and 0.038 mg m^{-3} (41 pairs), with a root mean square error of 0.036 and 0.020 mg m^{-3} for A1 and A2, respectively. The remote sensing observations generally overestimated at low Chl *a* and missed most high Chl *a*, compared with Bio-Argo data (see Figure 3). Previous studies also indicated that satellite remote sensing Chl *a* are usually higher than in situ measurements via survey ships in the SCS [e.g., *Tang et al*., 2004; *Shang et al*., 2014]. The maximum Chl *a* observed by A1 was near 1.8 mg m^{-3} in winter (Figure 3). High Chl *a* was also captured before by satellite remote sensing data (3.0 mg m^{-3}) and field survey (2.17 mg m^{-3}) in the northern SCS basin [*Tang et al*., 1999; *Shen et al*., 2008]. Therefore, the Chl *a* measurements by Bio-Argo floats are acceptable for this study although there must be some uncertainty described previously.

2.3. Identification of Eddies

The sea level anomaly (SLA) data have been widely used to identify and track mesoscale eddies. The SLA data set adopted in this work is an up-to-date delayed-time daily product generated by the Developing Use of Altimetry for Climate Studies (DUACS) system and distributed by the Archiving, Validation, and Interpretation of Satellite Oceanographic data (AVISO) project (ftp://ftp.aviso.oceanobs.com). It has been mapped to global Mercator grids with a 1/4° × 1/4° spatial resolution.

The eddy identifying and tracking methods applied in this paper are similar to those of *Chaigneau et al*. [2009] and have been used in *Zhang et al*. [2015a]. Two steps are taken to identify eddies: (1) searching the centers of all possible eddies and (2) finding their edges. The SLA contours are plotted with a uniform

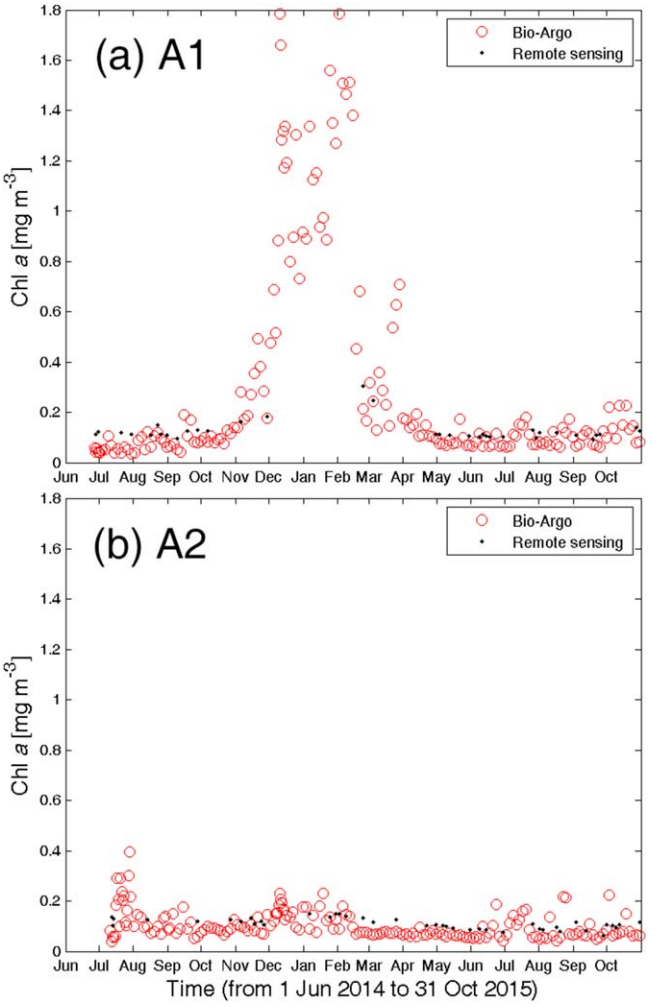

Figure 3. Comparison between the remote sensing Chl *a* and the Chl *a* at 5 m depth obtained by Bio-Argo floats (a) A1 and (b) A2. The remote sensing Chl *a* was the average value in a 0.4° × 0.4° box centered by the location of a float observation.

interval of 1 cm. Here the geometric center weighted by absolute SLA within an innermost closed contour is considered to be the center of a possible eddy. All closed contours surrounding each center are discovered, among which only those whose SLA values vary monotonously outward from the eddy center belong to the eddy. The outermost closed contour of the eddy is taken as the eddy edge. Only eddies whose amplitudes (the SLA difference between the center and the edge) are not less than 2 cm are reserved.

2.4. Wind Data and Wind Effects

Wind data used in this work were obtained from the National Climatic Data Center of National Oceanic and Atmospheric Administration (NOAA), USA (http://www.ncdc.noaa.gov/oa/rsad/air-sea/seawinds.html). This wind data set was generated by blending wind speed observations from multiple satellites and wind directions from the NCEP Reanalysis 2 [*Zhang et al*., 2006]. It is globally gridded on a mesh of 0.25° in both latitude and longitude. Several time resolutions (6 hourly, daily, monthly, and climatological monthly) were made to meet different needs and only daily wind fields were chosen to match the Bio-Argo observations described previously. Aside from the above one, there were another two global blended wind data sets: one was merged from QuikSCAT wind observations and ECMWF wind analyses; the other was merged from QuikSCAT winds and NCEP wind reanalyses. *Bentamy et al*. [2009] compared these three blended wind data sets with in situ observations from buoys, research vessels, and QuikSCAT scatterometer during the period of 2005–2006. They showed that the speeds and directions of blended wind data are in good agreement with in situ observations and concluded that these blended winds are appropriate for examining mesoscale air-sea interaction processes at both global and regional scales. Unfortunately, only the first blended wind data set is available after QuikSCAT satellite failed in 23 November 2009. Given that our study area is located in the open SCS basin away from coastlines, this blended wind set is certainly suitable for this work.

Wind effects on the upper ocean include vertical mixing (mechanical stirring, entrainment) and Ekman pumping (wind-driven upwelling or downwelling) which may affect the transport and distribution of nutrients [*Wang et al*., 2010; *Liu et al*., 2013; *Tang et al*., 2014]. Wind-driven vertical mixing depends on wind stress (vertical transfer of horizontal momentum from the atmosphere to the ocean). Wind stress can be parameterized by a quadratic law [*Zhang et al*., 2010]:

$$\tau = \rho_a C_d |\mathbf{W}| \mathbf{W}, \quad (1)$$

where τ is the wind stress vector; ρ_a is the density of air; C_d is the wind stress coefficient (drag coefficient);

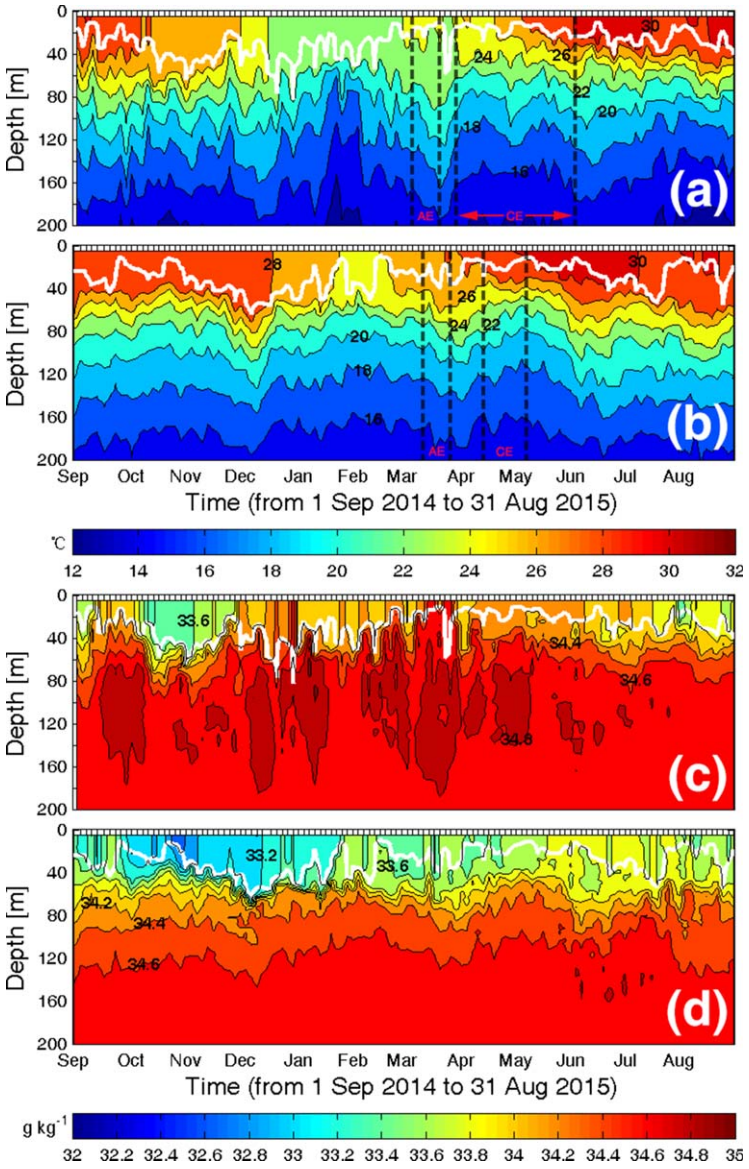

Figure 4. Time series of (a, b) conservative temperature and (c, d) absolute salinity profiles obtained by Bio-Argo floats (a, c) A1 and (b, d) A2. The white curve denotes the mixed layer depth. The interval of temperature contours is 2°C, and the interval of salinity contours is 0.2 g kg^{-1}. AE (CE) marks the period when the Bio-Argo float met an anticyclonic eddy (a cyclonic eddy). The dashed lines before and behind AE (CE) denote the beginning and ending of the period.

and **W** is the wind vector at 10 m height above the sea surface. Following *Zhang et al.* [2010], the wind stress coefficient was calculated by the following formula:

$$C_d \times 10^3 = \begin{cases} 1.052, & |\mathbf{W}| \le 6\,\mathrm{m\,s^{-1}} \\ 0.638 + 0.069|\mathbf{W}|, & 6 < |\mathbf{W}| < 30\,\mathrm{m\,s^{-1}} \\ 2.708, & |\mathbf{W}| \ge 30\,\mathrm{m\,s^{-1}} \end{cases}. \quad (2)$$

It is impossible to directly calculate real wind-driven mixing without current shear data; however, the magnitude of wind speed roughly indicates entrainment strength according to laboratory experimental results and simplified theoretical results: larger wind speed would cause stronger mixing in the surface layer because more kinetic energy is input for mixing from winds [*Kraus and Turner*, 1967; *Haney and Davies*, 1976; *Price*, 1981]. Ekman pumping (W_E) was estimated by the formula as follows:

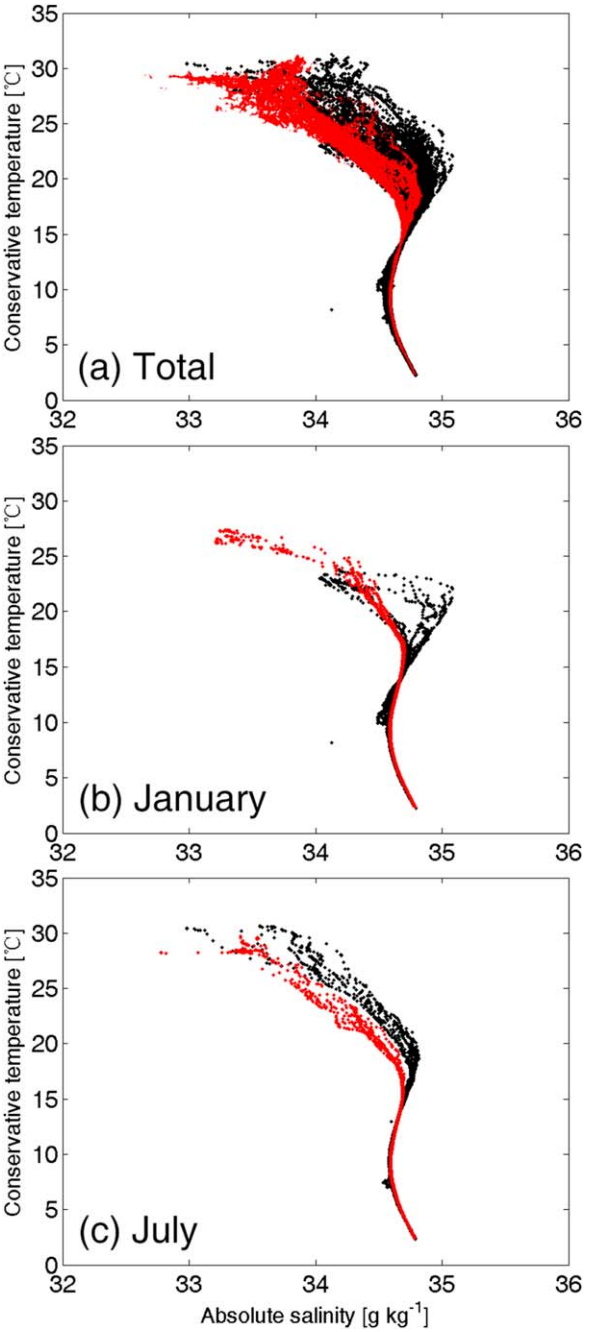

Figure 5. T-S diagram of water masses in the north (black) and in the center (red) of the SCS basin: (a) total observations from September 2014 to August 2015; (b) observations in January 2015; and (c) observations in July 2015.

$$W_E = \frac{1}{f\rho_w}\left(\frac{\partial \tau_y}{\partial x} - \frac{\partial \tau_x}{\partial y}\right), \quad (3)$$

$$f = 2\omega \sin\theta, \quad (4)$$

where τ_x and τ_y are the east and north components of wind stress, respectively, and θ is the latitude in degree. Here seawater density (ρ_w) and angular speed of the earth's rotation (ω) were set to 1020 kg m^{-3} and 7.292 $\times$ 10^{-5} s^{-1}, respectively.

3. Results and Discussion

3.1. Temperature and Salinity Variations

In the open SCS, the temporal variability of temperature and salinity was large in the upper 200 m layer (Figure 4) and small below the upper 200 m layer (data not shown). Based on the observations obtained by A1 in the northern SCS basin, the standard deviations of temperature and salinity were larger than 0.665°C and 0.028 g kg^{-1}, respectively, in the upper 200 m layer while they were smaller than 0.648°C and 0.027 g kg^{-1}, respectively, below the 200 m depth. There was a similar pattern in the observations of A2 in the central SCS basin. In the upper layer, both temperature and salinity experienced more variations in the northern basin than in the central basin. The mean standard deviation of temperature (salinity) in A1 observations was 1.486°C (0.142 g kg^{-1}), larger than 1.095°C (0.126 g kg^{-1}) in A2 observations. The salinity was higher almost throughout the year, and the temperature in winter (December to February) and spring (March to May) was lower in the north than the counterparts in the center (Figures 4 and 5).

The SCS is strongly influenced by the East Asian monsoon, northeasterly winds prevailing in winter and southwesterly winds in summer (June to August) [*Chu et al.*, 1999; *Zhang et al.*, 2015b]. In the mixed layer (Figure 3), the average temperature was lowest in winter due to strong wind mixing and negative net heat flux whereas it was highest in summer due to positive net heat flux dominating over wind mixing [*Qu*, 2001; *Duan et al.*, 2012; *Zhang et al.*, 2012]. In the subsurface layer (defined as the layer from the MLD to 200 m depth in this work), isotherms fluctuated up and down with time (Figure 4). Figure 4a shows that in the north, the isotherm of 18°C rose from approximately 160 m depth in December 2014 to above 120 m and reached the shallowest depth of 60 m in January 2015, indicating a significant shoaling of the isotherm. After that, the isotherm dropped down and returned to approximately 160 m depth by the end of March. Another two obvious isotherm shoaling processes happened during the periods from April to May and from June to August. In the center, two similar isotherm shoaling

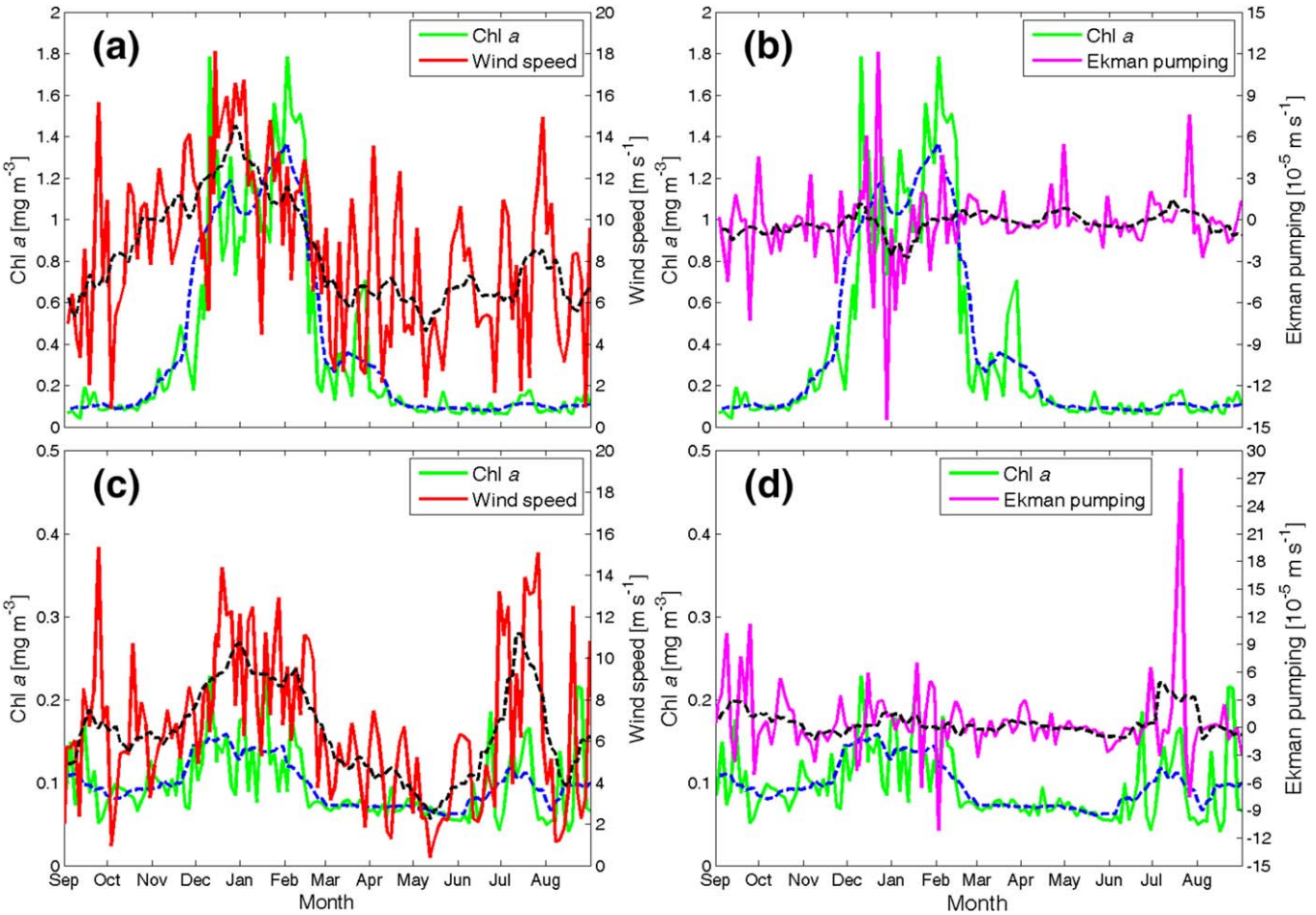

Figure 6. Time series of Chl *a*, wind speed, and Ekman pumping. The values of Chl *a* were the observations at 5 m depth from Bio-Argo floats (a, b) A1 and (c, d) A2. Wind speed and Ekman pumping were calculated from a daily remote sensing wind data set with a spatial resolution of 0.25° × 0.25°. Each value of wind speed in (a, c) or Ekman pumping in (b, d) was the average value in a 1° × 1° box centered by the corresponding point of Chl *a*. The black dashed curve denotes the 30 day running mean of wind speed in (a, c) or Ekman pumping in (b, d), and the blue one denotes the 30 day running mean of Chl *a*. It should be noted that the scales of Chl *a* and Ekman pumping in Figures 6c and 6d are different from their counterparts in Figures 6a and 6b.

processes occurred during the periods from December 2014 to March 2015 and from April to June (Figure 4b).

It is clear in Figure 4c that salty waters appeared intermittently in the subsurface layer in the northern basin from September 2014 to May 2015. Because their salinity was higher than that at 200 m depth, they could come not directly from the depths but via horizontal advection from other area. Their appearance time, high salinity, and sporadic features are consistent with the well-known Kuroshio water intrusion into the northern SCS through the Luzon Strait [*Yuan et al.*, 2006; *Yuan et al.*, 2014; *Zhang et al.*, 2015b]. Kuroshio intrusion is strongest in winter and successively becomes weaker during the spring, autumn, and summer [*Yuan et al.*, 2014]. Figure 5b shows that there were two different mater masses in January in the north. One water mass with high temperature and high salinity confirms the existence of Kuroshio intrusion water which has different properties from the SCS water [*Gong et al.*, 1992; *Liu et al.*, 2013]. Kuroshio intrusion appears as a transient event rather than a persistent circulation pattern [*Yuan et al.*, 2006; *Zhang et al.*, 2015b]. The salty intrusion water, sometimes trapped in the eddies shed from Kuroshio loop current in the Luzon Strait, can move westward along the continental slope of the northern SCS [*Yuan et al.*, 2006]. Interestingly, A1 was just in the pathway of westward-moving Kuroshio water during the study period. Figure 1 shows that A1 wandered in the northeastern SCS west of the Luzon Strait in the autumn (September to November) of 2014 and afterward it moved westward near the isobath of 200 m. Its maximum observation depth of each profile was deeper than 800 m (data not shown). These indicate that A1 traveled along the

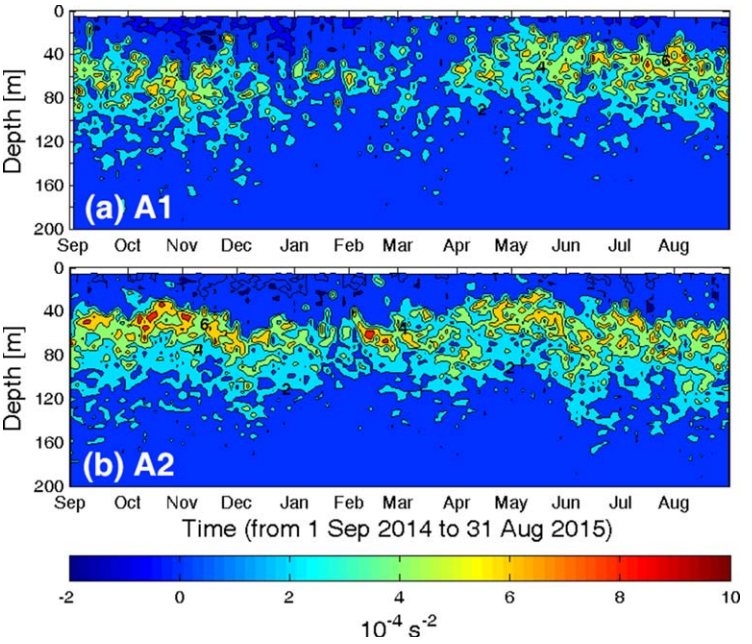

Figure 7. Time series of buoyancy (Brunt-Väisälä) frequency square (N^2) derived from the observations by Bio-Argo floats (a) A1 and (b) A2. The interval of N^2 is 2×10^{-4} s^{-2}.

continental slope in the northern SCS during northeasterly wind prevailing seasons, which is consistent in both time and space with the westward migration path of Kuroshio intrusion water [*Xue et al.*, 2004; *Qu et al.*, 2007; *Wu and Hsin*, 2012]. Hydrographic observations and modeling results have shown that Kuroshio water can intrude farther into the SCS through the Luzon Strait during the period when northeasterly wind prevails, and Kuroshio intrusion current flow westward along the continental slope [*Xue et al.*, 2004; *Wu and Hsin*, 2012]. *Qu et al.* [2007] remarked that Kuroshio intrusion water from the Luzon Strait has apparent influence along the continental slope in the northern SCS. Additionally, no such intermittent high salinity patches appearing in the center (see Figure 4d) further confirmed that the high salinity waters observed in the north originated from the Kuroshio water.

The change of temperature vertical structure is mainly caused by the combination of wind mixing, net surface heat flux, Ekman pumping, and eddy activities in the SCS [*Liu et al.*, 2000, 2001; *Qu et al.*, 2007; *Hao et al.*, 2012]. Negative heat flux produces a low SST whereas positive heat flux induces a high SST [*Qu*, 2001; *Duan et al.*, 2012]. In the winter, mean wind speed was 11.6 m s^{-1} in the northern basin and 10.0 m s^{-1} in the central basin (Figures 6a and 6c). Strong wind mixing may entrain deep colder and denser water into mixed layer [*Qu et al.*, 2007]. Figure 3 shows that the SST decreased to lower than 24°C (26°C) in the north (center) in winter. Surface cooling can induce and maintain vertical convection because it increases the density at the sea surface and makes upper layer water instable [*Qu et al.*, 2007; *Duan et al.*, 2012]. Ekman pumping changed its direction (upward and downward) frequently with time (Figures 6b and 6d). The 30 day running mean data indicate that in the north, the net value of Ekman pumping was positive (upward) in early December and February, but negative (downward) in late December and January; in the center, net Ekman pumping was positive for most of the winter. *Qu et al.* [2007] pointed out that wind mixing and cooling convection are dominant in the seasonal variation of isothermal depth in the northern SCS basin while Ekman pumping cannot be neglected, particularly in summer when wind becomes weak and SST is high. Kuroshio intrusion water with high salinity and high temperature could influence the temperature structure in the northern SCS during its westward migration [*Liu et al.*, 2001; *Qu et al.*, 2007]. *Liu et al.* [2001] demonstrated that the vertical displacement of thermocline in the northern SCS was closely related to Kuroshio intrusion. *Qu et al.* [2007] indicated that the Kuroshio intrusion through the Luzon Strait may play a role in the change of isothermal depth. Strong vertical convection corresponds to weak stratification, indicated by small N^2 [*Olbers et al.*, 2012]. On average, the smallest N^2 occurred in the winter of the study period (Figure 7), implying a weakest stratification and strong convection. The N^2 was lower in the north than in the center (Figure 7) because of the combined function of larger wind speed (Figure 6), lower surface temperature, and saltier Kuroshio intrusion water (Figure 4).

Eddy activities could also induce vertical displacement of isotherms. As a significant feature, the SLA is positive in an anticyclonic eddy whereas it is negative in a cyclonic eddy [*McGillicuddy et al.*, 2007]. During the period from 7 March to 22 March, an anticyclonic eddy passed A1 (Figure 8). Figure 9a shows that during this period the SLA was positive and the isotherm of 18°C deepened from 130 m to near 170 depth. After

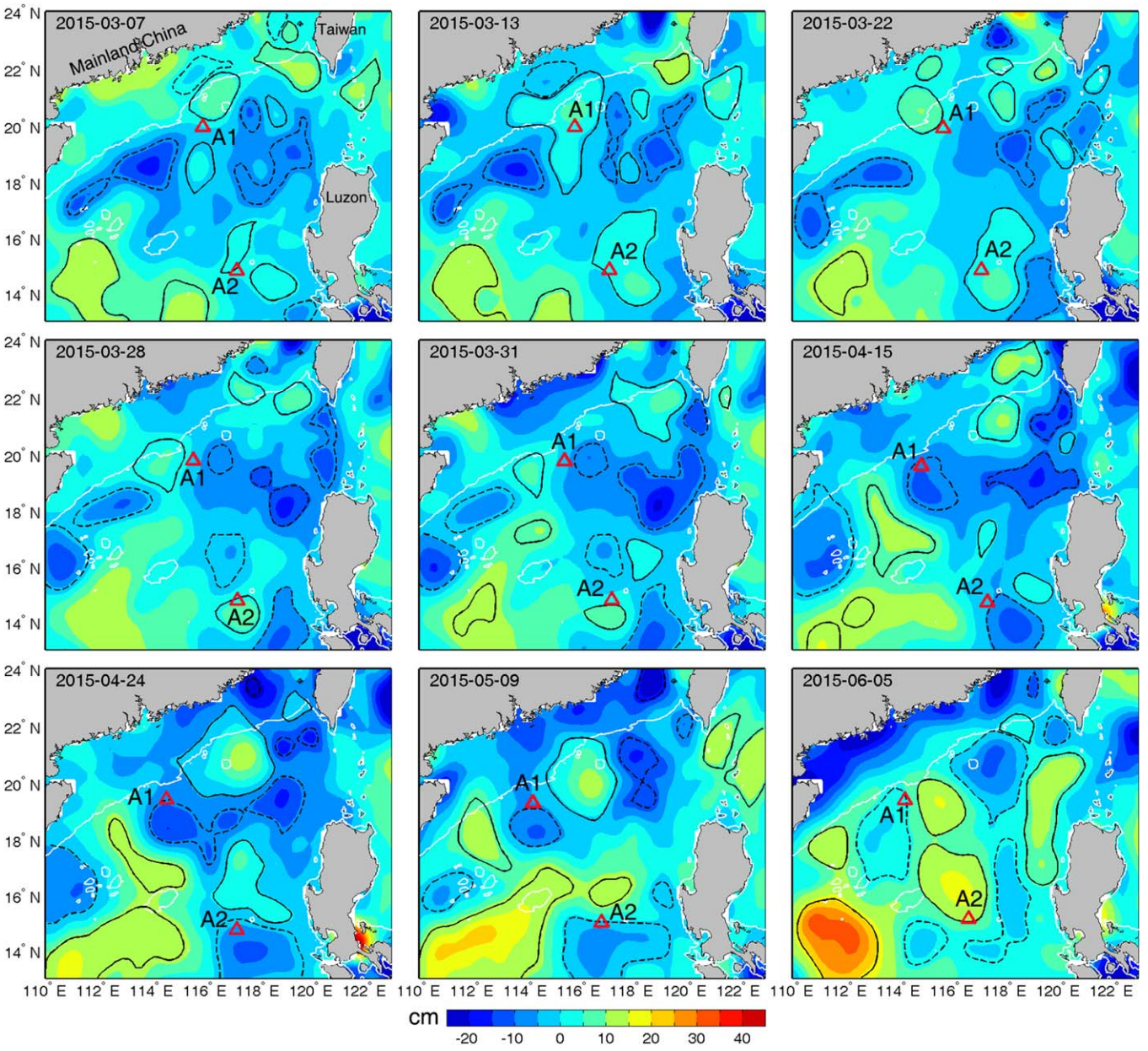

Figure 8. Eddies and the locations (red triangles) of Bio-Argo floats A1 and A2. The black solid (dashed) contours are the edges of anticyclonic (cyclonic) eddies. The white solid lines are the isobaths of 200 m. Colors denote sea level anomaly (SLA) values. For the visual integrity of eddies near 200 m isobaths, the SLA map in areas shallower than 200 m is shown also, although the signal in these areas was likely contaminated by tides.

A1 left the eddy, the SLA decreased to zero and the isotherm shoaled (Figure 9a). From 31 March to 5 June, A1 met a cyclonic eddy and then traveled with it (Figure 8). Accordingly the SLA became negative and the isotherm rose up to 100–130 m layer (Figure 9a). These two events coincided with the deepening and shoaling of isotherms during the two periods (Figure 4a), respectively. Similarly, A2 was inside an anticyclonic eddy with positive SLA during 13–28 March, corresponding to the descent (from 120 to 140 m depth) of the 18°C isotherm, whereas from 15 April to 9 May, it was caught by a cyclonic eddy with negative SLA and the isotherm went up to about 110 m depth (Figures 8 and 9b). The correlation coefficient between the depth of 18°C isotherm and SLA is 0.556 for A1 observations and 0.567 for A2 with 99.9% confidence level. This indicates that eddies played an important role in the vertical displacement of isotherms in the open SCS. The influence of eddies is sporadic and intraseasonal [*Liu et al*., 2001], which is different from the seasonal effects of monsoon winds, net surface heat flux, and Ekman pumping [*Qu et al*., 2007]. In the open

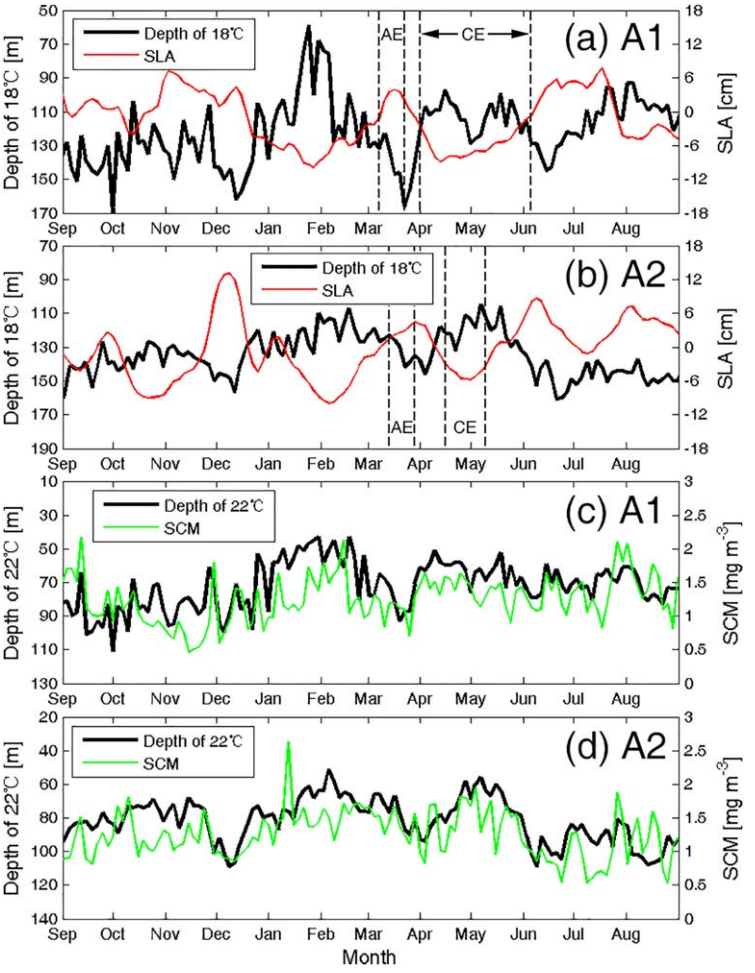

Figure 9. Time series of the depth of 18°C isotherm, SLA, depth of 22°C isotherm, SCM in relation to Bio-Argo floats A1 and A2. AE (CE) marks the period when the Bio-Argo float met an anticyclonic eddy (a cyclonic eddy). The dashed lines before and behind AE (CE) denote the beginning and ending of the period, respectively. Note that in Figure 9c, the values of the SCM during winter are the maximum Chl *a* in the surface layer.

SCS, monsoon winds, net surface heat flux, and Ekman pumping mainly affect the annual variation of temperature structure [*Chu et al.*, 1999; *Liu et al.*, 2001; *Qu et al.*, 2007].

3.2. Subsurface Chlorophyll Maximum

Figure 10 shows that high Chl *a* ($\geq$0.2 mg m^{-3}) was limited to the layer above 140 m in both northern and central parts of the SCS basin during the study period. The SCM was clear and prominent, except it was replaced by surface layer phytoplankton bloom with high Chl *a* in winter in the north (Figure 10). The depth of the SCM was usually below the MLD. In the northern part, the depth of the SCM ranged from 29 to 81 m during the study period except the winter, and its mean value and standard deviation were 61.3 and 11.2 m, respectively. In the central part, the SCM depth varied between 48 and 96 m, and its annual mean was 67.4 m with a standard deviation of 9.6 m. On average, it was shallower in the winter than in the summer (Table 1). The SCM was permanent in the center of the SCS basin but it was not in the north where there was actually no SCM in winter (Figure 10). In the winter of 2010, no DCMs were observed at many sampling stations in the northern SCS either [*Chen et al.*, 2013].

Without regard to the imprecision of converting chlorophyll fluorescence to Chl *a*, the Chl *a* depends on phytoplankton concentration and the ratio of Chl *a* to phytoplankton carbon, which are regulated by nutrient supply and light availability [*Liu et al.*, 2002; *Cullen*, 2015]. More available nutrient and light are responsible for higher Chl *a* and then larger SCM [*Mignot et al.*, 2014]. The euphotic zone depth is deeper than the top of the nutricline throughout the year in the SCS basin [*Tseng et al.*, 2005; *Chen and Chen*, 2006]. The mean depth of the SCM observed by A2 coincides with the tops of the nutricline (50–70 m) presented by *Tseng et al.* [2005]. These suggest that the magnitude of the SCM is mostly determined by the level of nutrient in the SCS basin.

Recent in situ observations by *Williams et al.* [2013] showed that the SCM depth corresponds to the base of thermocline as well as steep nitrate gradient. In the open SCS basin, the thermocline depth can be indicated by the depth of the 22°C [*Liu et al.*, 2001]. Figures 4 and 10 display that the isotherm of 22°C is just below (very close to) the depth of the SCM in both the northern and central basins. Here we used the vertical displacement of the 22°C isotherm to reflect the change of thermocline and available nutrients, resulted from the combined effects of all physical processes described previously. Figures 9c and 9d show that the values of the SCM are basically consistent with the depths of the isotherm. The correlation coefficient between

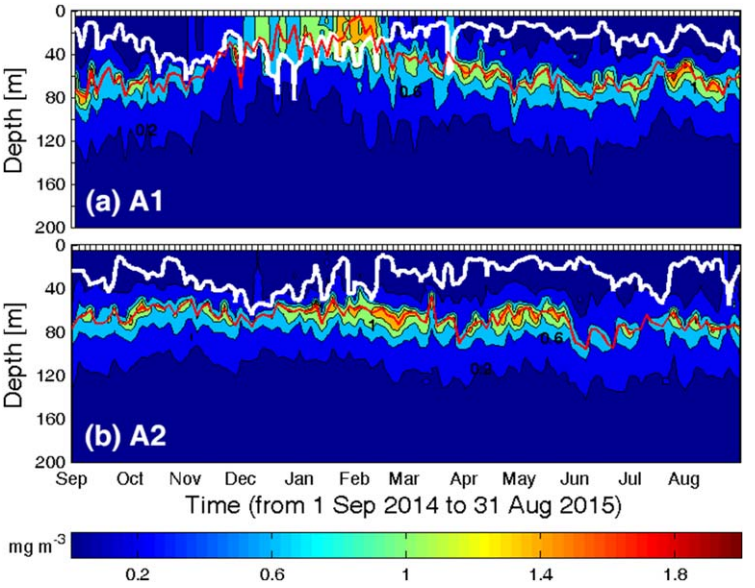

Figure 10. Time series of Chl *a* profiles obtained by Bio-Argo floats (a) A1 and (b) A2. The white curve denotes the MLD, and the red one denotes the depth of maximum Chl *a*. The interval of contours is 0.4 mg m^{-3}.

them is −0.444 in the north and −0.538 in the center of the SCS basin, indicating a significant correlation with 99.9% confidence level (121 samples). This suggests that the shoaling of the isotherm (thermocline) tended to provide more nutrients for the growth of phytoplankton, resulting in a higher SCM.

Because the ratio of nitrogen to phosphorus (N/P) is smaller than the corresponding Redfield ratio, the deep basin of the SCS is nitrogen limited for phytoplankton growth [*Chen et al.*, 2004]. Both in situ observations and enrichment experiments have shown that phytoplankton growth in the SCS is limited by nitrogen rather than light intensity and grazing by zooplankton [*Chen et al.*, 2004, 2006]. Figures 11e and 11f show the climatological monthly mean nitrate concentration profiles which are higher at depth in January (representing winter) than in July (summer) in both northern and central parts of the SCS basin. Observed by A2 in the central SCS basin, the SCM was larger in winter and spring, compared with that in summer and autumn (Figure 10b and Table 1). *Chen and Chen* [2006] observed that relatively shallow nitracline in winter makes the waters highly productive in the SCS.

3.3. Surface Layer Chlorophyll Variability

Surface layer Chl *a*, denoted by observations at 5 m depth, was higher and more variable in the north than in the center of the open SCS (Figure 10 and Table 1). The mean value and corresponding standard deviation in the north were 0.32 and 0.43 mg m^{-3}, about three and seven times the counterparts (0.11, 0.06 mg m^{-3}) in the center, respectively. In the north, the largest value of seasonally averaged Chl *a* concentration (1.07 mg m^{-3}) occurred in winter, followed by spring (0.19 mg m^{-3}), autumn (0.16 mg m^{-3}), and summer (0.10 mg m^{-3}). The winter phytoplankton bloom appeared in the entire mixed layer (Figure 10a). The ratio of Chl *a* between winter and summer is 10.7, larger than those (approximately 3) obtained from remote sensing data by *Shen et al.* [2008] and from in situ observations by *Chen and Chen* [2006]. In the center, surface layer Chl *a* was very low in the study period and only in winter the averaged value (0.14 mg m^{-3}) was above 0.10 mg m^{-3} (Table 1). The above seasonal cycle of Chl *a* in the SCS basin is qualitatively in agreement with previous results obtained from remote sensing data [*Shen et al.*, 2008; *Palacz et al.*, 2011] and from in situ observations [*Chen and Chen*, 2006; *Liu et al.*, 2007] in the open SCS.

The supply of nutrients is a controlling factor for the growth of phytoplankton in the surface layer where enough light is readily available [*Tang et al.*, 2014]. Surface layer nutrient supply is related to physical processes: vertical mixing, upwelling, vertical convection, and advection. Wind-driven vertical mixing and upwelling can bring nutrient-rich deep water to the surface layer [*Wang et al.*, 2010; *Duan et al.*, 2012; *Yang et al.*, 2012]. As seen in Figure 6, higher Chl *a* seems to coincide with stronger wind speed. The correlation coefficient between 30 day running filtering wind

Table 1. Seasonally Averaged Depth (m) and Values (mg m^{-3}) of the SCM and Surface Layer Chl *a* (mg m^{-3}) Calculated From Observations of Bio-Argo Floats

Bio-Argo	Parameter	Autumn	Winter	Spring	Summer
A1	SCM (depth/value)	61.77/1.06		56.71/1.30	65.51/1.37
	Surface layer (5 m)	0.16	1.07	0.19	0.10
A2	SCM (depth/value)	62.97/1.20	61.79/1.39	67.06/1.43	77.19/1.00
	Surface layer (5 m)	0.10	0.14	0.07	0.09

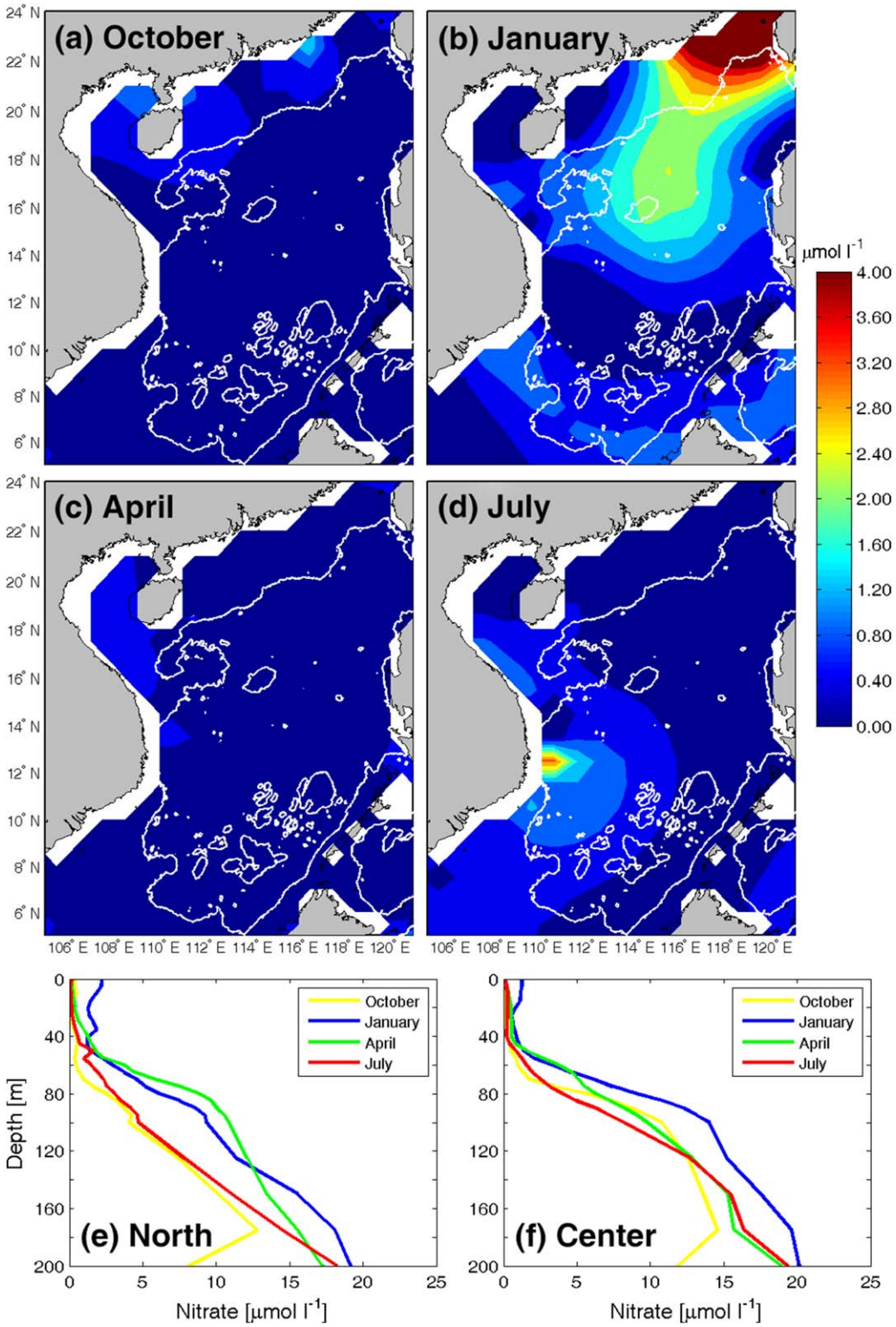

Figure 11. (a–d) Distribution of nitrate at 5 m depth, (e) vertical profiles of nitrate averaged in the domain shown in Figure 1b, and (f) vertical profiles of nitrate averaged in the domain shown in Figure 1c, based on the climatological monthly data of the World Ocean Atlas (WOA V2 2013). This climatological data set has a vertical interval of 5 m in the top layer of 0-100 m and 25 m below the top layer, and a horizontal resolution of 1° in both latitude and longitude. The white curves in Figures 11a–11d denote the isobath of 1000 m.

Table 2. Area-Averaged Nitrate Concentration (μmol L^{-1}) in the North (Shown in Figure 1b) and Center (Shown in Figure 1c) of the SCS Basin, Based on the Climatological Monthly Data (WOA V2 2013)

	Parameter	October	January	April	July
North	Mean in 0–20 m layer	0.327	1.766	0.228	0.118
	Mean in 20–50 m layer	0.341	1.435	1.088	0.606
	At 5 m depth	0.333	2.149	0.164	0.056
	Minimum below 5 m depth and its depth (m)	0.187/30	1.196/45	0.236/10	0.099/10
Center	Mean in 0–20 m layer	0.080	1.099	0.302	0.209
	Mean in 20–50 m layer	0.208	0.836	0.740	0.347
	At 5 m depth	0.080	1.238	0.213	0.196
	Minimum below 5 m depth and its depth (m)	0.027/30	0.485/25	0.339/10	0.202/40

speed and Chl *a* was 0.824 (127 samples) and 0.812 (130 samples) with a significance level of 99.9% in the north and center, respectively. By contrast, the correlation coefficient between Chl *a* and local Ekman pumping was very low (−0.061 for A1, 0.171 for A2). *Palacz et al.* [2011] also found from remote sensing data that Chl *a* correlates significantly and positively with surface wind speed, while no similar correlation exists between Chl *a* and wind stress curl. *Tang et al.* [2014] indicated that wind stirring is more important for surface Chl *a* than wind stress curl. These findings suggest that wind-driven vertical mixing contributed more to the growth of surface layer Chl *a* than Ekman pumping induced by wind stress curl in the open SCS. In addition to wind effects, the vertical convection due to surface cooling mentioned previously also contributed to higher Chl *a* in winter [*Duan et al.*, 2012; *Tang et al.*, 2014]. Salty Kuroshio water intrusion potentially enhanced this process in the northern SCS basin [*Liu et al.*, 2000; *Qu et al.*, 2007]. The correlation coefficient between Chl *a* and temperature at 5 m depth was −0.7566 (127 samples) in the north, while it was −0.3101 (130 samples) in the center. Although both have a significance level of 99.9%, the correlation is higher in the north. Based on remote sensing surface Chl *a* and SST data, *Tang et al.* [2014] demonstrated that a significant correlation between Chl *a* and SST only occurs in the northern SCS.

From the perspective of multiyear average, climatological monthly data (Figure 11) show that in January, nitrate concentration decreases southwestward from the southern Taiwan Strait and adjacent shallow continental shelf. Higher nitrate concentration covers the northern basin of the SCS, compared with that in the southern basin (Figure 11b). This is consistent with previous results that wind-induced circulation as well as volume transport in the Taiwan Strait and the northern SCS is southward or southwestward in winter [*Chu et al.*, 1999; *Wu and Hsin*, 2005; *Zhang et al.*, 2014], which can drive nutrient-rich water from the East China Sea into the northern SCS through the Taiwan Strait [*Chen 2008; Chen et al.*, 2013]. The mean nitrate concentration in the layer of 0–20 m is 1.766 μmol l^{-1}, higher than 1.435 μmol l^{-1} in the layer below (20–50 m), in the north (Figure 11e and Table 2). Similar results also appear in the center (Figure 9f and Table 2). Nitrate concentration generally increases with depth in the SCS [*Takahashi and Hori*, 1984]. If nitrate in the upper layer all came from the lower layer, the nitrate concentration in the upper layer would be no higher than that in the lower layer, just similar to the case in April and July (Figures 11e and 11f, Table 2). In January, nitrate concentration is 2.149 μmol l^{-1} at 5 m depth, nearly twice the minimum (1.196 μmol l^{-1}) below 5 m depth (Table 2). Given that the contribution of deep water to nitrate concentration at 5 m depth is no more than 1.196 μmol l^{-1}, it could be estimated that the nitrate from deep water contributes 55.7% (1.196/2.149) or less to the nitrate at 5 m. In the central SCS basin, this value reduces to no more than 39.2% (0.485/1.238). These indicate that the contribution by horizontal advection to nitrate concentration at 5 m in January is at least 44.3% in the north and 60.8% in the center. Although the relative contribution of horizontal advection is higher in the center, the absolute value (the value at 5 m depth minus the minimum below) is higher (0.953 μmol l^{-1} versus 0.753 μmol l^{-1}) in the north, which is consistent with horizontal change trend shown in Figure 11b. In October, although mean nitrate concentration is lower in the upper layer than in the lower layer, a lower nitrate concentration at 30 m depth than that at 5 m depth suggests a weak surface horizontal advection existing both in the north and in the center (Table 2). In April and July, no appreciable nitrate advection happens in the surface layer of the study region since the nitrate concentration basically increases with depth (Figures 11e and 11f, Table 2). Previous findings indicated that in winter strong northeasterly wind drives water to flow southward through the Taiwan Strait, resulting in southward volume transport [*Wu and Hsin*, 2005; *Zhang et al.*, 2014], thus nutrients may be transported into the northern SCS from the East China Sea [*Chen*, 2008; *Chen et al.*, 2013]. Field surveys in the northern SCS showed that surface nutrient concentration decreased from shelf to slope and basin in January 2010 while no evident cross-

shelf gradient appeared in July to August 2009 [*Chen et al*., 2013]. These results are consistent with the above results obtained from climatological data. Therefore, horizontal advection may supply additional nitrogen to enhance the winter phytoplankton bloom in the northern SCS basin. Note that the climatological monthly data describe only average state at the seasonal timescale, excluding interannual variations. However, seasonal signals in monsoon winds, surface circulation, nutrient concentration, and Chl *a* are dominant over interannual changes in the SCS [*Wu et al*., 1998; *Palacz et al*., 2011; *Liu et al*., 2013], which suggests that the seasonal variation of the SCS environment in an individual year may be different but do not depart much from climatological monthly state in the open SCS. The contribution of eddies to the winter bloom was not considered here because A1 stayed outside eddies almost throughout the winter except only one profile at the edge of a weak cyclonic eddy (figures omitted).

4. Conclusions

The observations of Bio-Argo floats during a 1 year study period of September 2014 to August 2015 were used to describe the spatial and temporal variability of Chl *a* in the open SCS. In the center of the SCS basin, there was a permanent SCM. The SCM was located in the depth range of 48–96 m with a mean depth of 67.4 m. The value of the SCM tended to vary inversely with the depth of the 22°C isotherm: large SCM corresponded to shallow isotherm and vice versa. This demonstrated that the SCM value was mainly determined by nutrient supply from depths. The upward displacement of nitrate-rich water was responsible for large SCM in winter and spring. In the north, the SCM disappeared in winter and was replaced by surface layer phytoplankton bloom.

Surface layer Chl *a* in the SCS basin was low except during the winter in the north. It had a significant correlation with wind speed and the SST. Strong wind forcing and surface cooling were the main physical drivers of high Chl *a* in winter because of their active effects on upward nutrient supply. Compared with the center of the SCS basin, stronger wind and lower SST as well as Kuroshio water intrusion in the north were more favorable for the upward supply of nutrients during the winter. Additionally, a large amount of nitrate was probably advected from the Taiwan Strait and shallow continental shelf to the northern basin. As a result, a significant winter surface layer phytoplankton bloom occurred in the north rather than in the center of the SCS basin.

It should be noted that some uncertainty is inevitable in the values of Chl *a* derived from chlorophyll fluorescence signals and synchronous in situ validation is impossible for fluorometers on autonomous platforms like Bio-Argo floats [*Mignot et al*., 2011; *Cullen*, 2015]. Notwithstanding the above problem, the spatial and temporal variations of Chl *a* observed by Bio-Argo floats with factory-calibrated sensors are credible and valuable to monitor the change of the ecological environment in the open SCS. Indicated by *Cullen* [2015], novel techniques and new approaches, as proposed by *Mignot et al*. [2011] and *Roesler and Barnard* [2013], are required to obtain more accurate values of in situ Chl *a* using sensors on autonomous profiling floats.

Acknowledgments
This work was jointly funded by the State Key R&D project (grant 2016YFA0601103), the National Natural Science Foundation of China (grants U1305231, 41276007, 41576100), President Research Award (2013121047), and the National Basic Research Program of China (grant 2015CB954002). The Bio-Argo data used were obtained from State Key Laboratory of Marine Environmental Science, Xiamen University (http://odc.xmu.edu.cn/BioArgo/Default.aspx). The daily remote sensing surface Chl *a* data were produced and distributed by the Ocean Biology Processing Group at NASA (http://oceandata.sci.gsfc.nasa.gov/). The daily wind data were taken from the National Climatic Data Center of National Oceanic and Atmospheric Administration (NOAA), USA (http://www.ncdc.noaa.gov/oa/rsad/air-sea/seawinds.html). The monthly climatological nitrate data were from the World Ocean Atlas (WOA V2 2013), provided by NOAA National Centers for Environmental Information (http://www.nodc.noaa.gov/OC5/woa13/woa13data.html). We appreciate two anonymous reviewers' constructive comments and helpful suggestions on the improvement of the manuscript.

References

Bentamy, A., D. Croize-Fillon, P. Queffeulou, C. Liu, and H. Roquet (2009), Evaluation of high-resolution surface wind products at global and regional scales, *J. Oper. Oceanogr.*, *2*, 15–27.

Bienfang, P. K., J. P. Szyper, and E. Laws (1983), Sinking rate and pigment responses to light limitation by a marine diatom: Implications to dynamics of chlorophyll maximum layers, *Oceanol. Acta*, *6*, 55–62.

Chaigneau, A., G. Eldin, and B. Dewitte (2009), Eddy activity in the four major upwelling systems from satellite altimetry (1992–2007), *Prog. Oceanogr.*, *83*, 117–123.

Chen, B., L. Zheng, B. Huang, S. Song, and H. Liu (2013), Seasonal and spatial comparisons of phytoplankton growth and mortality rates due to microzooplankton grazing in the northern South China Sea, *Biogeosciences*, *10*, 2775–2785.

Chen, C. C., F. K. Shiah, S. W. Chung, and K. K. Liu (2006), Winter phytoplankton blooms in the shallow mixed layer of the South China Sea enhanced by upwelling, *J. Mar. Syst.*, *59*, 97–110.

Chen, C. T. A. (2008), Distributions of nutrients in the East China Sea and the South China Sea connection, *J. Oceanogr.*, *64*, 737–751.

Chen, C. T. A., S. Jan, T. H. Huang, and Y. H. Tseng (2010), Spring of no Kuroshio intrusion in the southern Taiwan Strait, *J. Geophys. Res.*, *115*, C08011, doi:10.1029/2009JC005804.

Chen, Y. L. L. (2005), Spatial and seasonal variations of nitrate-based new production and primary production in the South China Sea, *Deep Sea Res., Part I*, *52*, 319–340.

Chen, Y. L. L., and H. Y. Chen (2006), Seasonal dynamics of primary and new production in the northern South China Sea: The significance of river discharge and nutrient advection, *Deep Sea Res., Part I*, *53*, 971–986.

Chen, Y. L. L., H. Y. Chen, D. M. Karl, and M. Takahashi (2004), Nitrogen modulates phytoplankton growth in spring in the South China Sea, *Cont. Shelf Res.*, *24*, 527–541.

Chu, P. C., and R. Li (2000), South China Sea isopycnal-surface circulation, *J. Phys. Oceanogr.*, *30*(9), 2419–2438.

Chu, P. C., N. L. Edmons, and C. Fan (1999), Dynamical mechanisms for the South China Sea seasonal circulation and thermohaline variabilities, *J. Phys. Oceanogr.*, *29*, 2971–2989.
Chekalyuk, A. M., F. E. Hoge, C. W. Wright, R. N. Swift, and J. K. Yungel (2000), Airborne test of laser pump-and-probe technique for assessment of phytoplankton photochemical characteristics, *Photosyn. Res.*, *66*, 45–56.
Cullen, J. J. (2015), Subsurface chlorophyll maximum layers: Enduring enigma or mystery solved, *Annu. Rev. Mar. Sci.*, *7*, 207–239.
Duan, R., K. Yang, Y. Ma, and T. Hu (2012), A study of the mixed layer of the South China Sea based on the multiple linear regression, *Acta Oceanol. Sin.*, *31*, 19–31.
Durham, W. M., and R. Stocker (2012), Thin phytoplankton layers: Characteristics, mechanisms, and consequences, *Annu. Rev. Mar. Sci.*, *4*, 177–207.
Fan, C., J. Wang, and J. Song (2010), Factors influencing the climatological mixed layer depth in the South China Sea: Numerical simulations, *Chin. J. Oceanol. Limnol.*, *28*, 1112–1118.
Fennel, K., and E. Boss (2003), Subsurface maxima of phytoplankton and chlorophyll: Steady-state solutions from a simple model, *Limnol. Oceanogr.*, *48*, 1521–1534.
Gong, G.-C., K.-K. Liu, C.-T. Liu, and S.-C. Pai (1992), Chemical hydrography of the South China Sea and a comparison with the West Philippine Sea, *Terr. Atmos. Ocean Sci.*, *3*, 587–602.
Gong, X., J. Shi, and H. Gao (2014), Modeling seasonal variations of subsurface chlorophyll maximum in South China Sea, *J. Ocean Univ. China*, *13*(4), 561–571, doi:10.1007/s11802-014-2060-4.
Green, R. E., A. S. Bower, and A. Lugo-Fernández (2014), First autonomous bio-optical profiling float in the Gulf of Mexico Reveals dynamic biogeochemistry in deep waters, *PLoS One*, *9*(7), e101658, doi:10.1371/journal.pone.0101658.
Haney, R. L., and R. W. Davies (1976), The role of surface mixing in the seasonal variation of the ocean thermal structure, *J. Phys. Oceanogr.*, *6*, 504–510.
Hao, J., Y. Chen, F. Wang, and P. Lin (2012), Seasonal thermocline in the China Seas and northwestern Pacific Ocean, *J. Geophys. Res.*, *117*, C02022, doi:10.1029/2011JC007246.
Hu, C., Z. Lee, and B. Franz (2012), Chlorophyll a algorithms for oligotrophic oceans: A novel approach based on three-band reflectance difference, *J. Geophys. Res.*, *117*, C01011, doi:10.1029/2011JC007395.
Hu, J., H. Kawamura, H. S. Hong, and Y. Qi (2000), A review on the currents in the South China Sea: Seasonal circulation, South China Sea Warm Current and Kuroshio intrusion, *J. Oceanogr.*, *56*, 607–624.
Huot, Y., and M. Babin (2011), Overview of fluorescence protocols: Theory, basic concepts, and practice, in *Chlorophyll a Fluorescence in Aquatic Sciences: Methods and Applications*, edited by D. J. Suggett, O. Prášil, and M. A. Borowitzka, pp. 31–74, Springer, Dordrecht.
Kraus, E. B., and J. S. Turner (1967), A one-dimensional model of the seasonal thermocline, *Tellus*, *19*, 98–106.
Lin, I. I., W. T. Liu, C. C. Wu, G. T. F. Wong, C. Hu, Z. Chen, W. D. Liang, Y. Yang, and K. K. Liu (2003), New evidence for enhanced ocean primary production triggered by tropical cyclone, *Geophys. Res. Lett.*, *30*(13), 1718, doi:10.1029/2003GL017141.
Liu, F., and C. Chen (2014), Seasonal variation of chlorophyll a in the South China Sea from 1997–2010, *Aquat. Ecosyst. Health Manage.*, *17*, 212–220.
Liu, H., J. Chang, C. M. Tseng, L. S. Wen, and K. K. Liu (2007), Seasonal variability of picoplankton in the Northern South China Sea at the SEATS station, *Deep Sea Res., Part II*, *54*, 1602–1616.
Liu, K. K., S. Y. Chao, P. T. Shaw, G. C. Gong, C. C. Chen, and T. Y. Tang (2002), Monsoon-forced chlorophyll distribution and primary production in the South China Sea: Observations and a numerical study, *Deep Sea Res., Part I*, *49*, 1387–1412.
Liu, K. K., L. W. Wang, M. Dai, C. M. Tseng, Y. Yang, C. H. Sui, L. Y. Oey, K. Y. Tseng, and S. M. Huang (2013), Inter-annual variation of chlorophyll in the northern South China Sea observed at the SEATS Station and its asymmetric responses to climate oscillation, *Biogeosciences*, *10*, 2013–7449.
Liu, Q. Y., H. J. Yang, and Q. Wang (2000), Dynamic characteristics of seasonal thermocline in the deep sea region of the South China Sea, *Chin. J. Oceanol. Limnol.*, *18*, 104–109.
Liu, Q., Y. Jia, P. Liu, and Q. Wang (2001), Seasonal and intraseasonal thermocline variability in the central South China Sea, *Geophys. Res. Lett.*, *28*, 4467–4470.
McGillicuddy, D. J., et al. (2007), Eddy/wind interactions stimulate extraordinary mid-ocean plankton blooms, *Science*, *316*, 1021–1026.
Mignot, A., H. Claustre, F. D'Ortenzio, X. Xing, A. Poteau, and J. Ras (2011), From the shape of the vertical profile of in vivo fluorescence to Chlorophyll-a concentration, *Biogeosciences*, *8*, 2391–2406.
Liu, H., J. Chang, C. M. Tseng, L. S. Wen, and K. K. Liu (2007), Seasonal variability of picoplankton in the Northern South China Sea at the SEATS station, *Deep Sea Res., Part II*, *54*, 1602–1616.
Liu, K. K., S. Y. Chao, P. T. Shaw, G. C. Gong, C. C. Chen, and T. Y. Tang (2002), Monsoon-forced chlorophyll distribution and primary production in the South China Sea: Observations and a numerical study, *Deep Sea Res., Part I*, *49*, 1387–1412.
Liu, K. K., L. W. Wang, M. Dai, C. M. Tseng, Y. Yang, C. H. Sui, L. Y. Oey, K. Y. Tseng, and S. M. Huang (2013), Inter-annual variation of chlorophyll in the northern South China Sea observed at the SEATS Station and its asymmetric responses to climate oscillation, *Biogeosciences*, *10*, 2013–7449.
Liu, Q. Y., H. J. Yang, and Q. Wang (2000), Dynamic characteristics of seasonal thermocline in the deep sea region of the South China Sea, *Chin. J. Oceanol. Limnol.*, *18*, 104–109.
Liu, Q., Y. Jia, P. Liu, and Q. Wang (2001), Seasonal and intraseasonal thermocline variability in the central South China Sea, *Geophys. Res. Lett.*, *28*, 4467–4470.
McGillicuddy, D. J., et al. (2007), Eddy/wind interactions stimulate extraordinary mid-ocean plankton blooms, *Science*, *316*, 1021–1026.
Mignot, A., H. Claustre, F. D'Ortenzio, X. Xing, A. Poteau, and J. Ras (2011), From the shape of the vertical profile of in vivo fluorescence to Chlorophyll-a concentration, *Biogeosciences*, *8*, 2391–2406.
Mignot, A., H. Claustre, J. Uitz, A. Poteau, F. D'Ortenzio, and X. Xing (2014), Understanding the seasonal dynamics of phytoplankton biomass and the deep chlorophyll maximum in oligotrophic environments: A bio-Argo float investigation, *Global Biogeochem. Cycles*, *28*, 856–876.
Olbers, D., J. Willebbrand, and C. Eden (2012), *Ocean Dynamics*, 704 pp., Springer, Dordrecht.
Palacz, A. P., H. Xue, C. Armbrecht, C. Zhang, and F. Chai (2011), Seasonal and inter-annual changes in the surface chlorophyll of the South China Sea, *J. Geophys. Res.*, *116*, C09015, doi:10.1029/2011JC007064.
Price, J. F. (1981), Upper ocean response to a hurricane, *J. Phys. Oceanogr.*, *11*, 153–175.
Qu, T. (2001), Role of ocean dynamics in Qu, T. (2001), Role of ocean dynamics in determining the mean seasonal cycle of the South China Sea surface temperature, *J. Geophys. Res.*, *106*, 6943–6955.
Qu, T., Y. Du, J. Gan, and D. Wang (2007), Mean seasonal cycle of isothermal depth in the South China Sea, *J. Geophys. Res.*, *112*, C02020, doi:10.1029/2006JC003583.

Roesler, C. S., and A. H. Barnard (2013), Optical proxy for phytoplankton biomass in the absence of photophysiology: Rethinking the absorption line height, *Methods Oceanogr.*, *7*, 79–94.
Sackmann, B. S., M. J. Perry, and C. C. Eriksen (2008), Seaglider observations of variability in daytime fluorescence quenching of chlorophyll-a in northeastern Pacific coastal waters, *Biogeosci. Discuss.*, *5*, 2839–2865, doi:10.5194/bgd-5-2839-2008.
Shang, S., L. Li, F. Sun, J. Wu, C. Hu, D. Chen, X. Ning, Y. Qiu, C. Zhang, and S. P. Shang (2008), Changes of temperature and bio-optical properties in the South China Sea in response to Typhoon Lingling, 2001, *Geophys. Res. Lett.*, *35*, L10602, doi:10.1029/2008GL033502.
Shang, S. L., Q. Dong, C. Hu, G. Lin, Y. H. Li, and S. P. Shang (2014), On the consistency of MODIS chlorophyll a products in the northern South China Sea, *Biogeosciences*, *11*, 269–280.
Shen, S., G. G. Leptoukh, J. G. Acker, Z. Yu, and S. J. Kempler (2008), Seasonal variations of chlorophyll a concentration in the northern South China Sea, *IEEE Geosci. Remote Sens. Lett.*, *5*(2), 315–319.
Shinoda, T., H. H. Hendon, and J. Glick (1998), Intraseasonal variability of surface fluxes and sea surface temperature in the tropical western Pacific and Indian Oceans, *J. Clim.*, *11*, 1685–1702.
Stacey, M. T., M. A. McManus, and J. V. Steinbuck (2007), Convergences and divergences and thin layer formation and maintenance, *Limnol. Oceanogr., 52 K.*, *39*, 217–226.
Taahashi, M., and T. Hori (1984), Abundance of picophytoplankton in the subtropical and tropical waters, *Mar. Biol.*, *79*, 177–186.
Tang, D. L., I. H. Ni, D. R. Kester, and F. E. Müller-Karger (1999), Remote sensing observations of winter phytoplankton blooms southwest of the Luzon Strait in the South China Sea, *Mar. Ecol. Prog. Ser.*, *191*, 43–51.
Tang, D. L., H. Kawamura, T. van Dien, and M. A. Lee (2004), Offshore phytoplankton biomass increase and its oceanographic causes in the South China Sea, *Mar. Ecol. Prog. Ser.*, *268*, 31–41.
Tang, S., F. Liu, and C. Chen (2014), Seasonal and intraseasonal variability of surface chlorophyll a concenTang, S., F. Liu, and C. Chen (2014), Seasonal and intraseasonal variability of surface chlorophyll a concentration in the South China Sea, *Aquat. Ecosyst. Health Manage.*, *17*, 242–251.
Tseng, C.-M., G. T. F. Wong, I.-I. Lin, C.-R. Wu, and K.-K. Liu (2005), A unique seasonal pattern in phytoplankton biomass in low-latitude waters in the South China Sea, *Geophys. Res. Lett.*, *32*, L08608, doi:10.1029/2004GL022111.
Wang, J. J., D. L. Tang, and Y. Sui (2010), Winter phytoplankton bloom induced by subsurface upwelling and mixed layer entrainment southwest of Luzon Strait, *J. Mar. Syst.*, *83*, 141–149.
Williams, C., J. Sharples, C. Mahaffey, and T. Rippeth (2013), Wind-driven nutrient pulses to the subsurface chlorophyll maximum in seasonally stratified shelf seas, *Geophys. Res. Lett.*, *40*, 5467–5472.
Wu, C.-R., and Y.-C. Hsin (2005), Volume transport through the Taiwan Strait: A numerical study, *Terr. Atmos. Oceanic Sci.*, *16*, 377–391.
Wu, C.-R., P.-T. Shaw, and S.-Y. Chao (1998), Seasonal and interannual variations in the velocity field of the South China Sea, *J. Oceanogr.*, *54*, 361–372.
Wu, C.-R., and Y.-C. Hsin (2012), The forcing mechanism leading to the Kuroshio intrusion into the South China Sea, *J. Geophys. Res.*, *117*, C07015, doi:10.1029/2012JC007968.
Wyrtki, K. (1961), Physical oceanography of the southeast Asian waters, *Naga Rep. 2*, pp. 1–195, Scripps Inst. of Oceanogr., San Diego, Calif.
Xing, X., A. Morel, H. Claustre, D. Antoine, F. D'Ortenzio, A. Poteau, and A. Mignot (2011), Combined processing and mutual interpretation of radiometry and fluorimetry from autonomous profiling Bio-Argo floats: Chlorophyll a retrieval, *J. Geophys. Res.*, *116*, C06020, doi:10.1029/2010JC006899.
Xue, H., F. Chai, N. Pettigrew, D. Xu, M. Shi, and J. Xu (2004), Kuroshio intrusion and the circulation in the South China Sea, *J. Geophys. Res.*, *109*, C02017, doi:10.1029/2002JC001724.
Yang, Y. J., T. Xian, L. Sun, and Y. F. Fu (2012), Summer monsoon impacts on chlorophyll-a concentration in the middle of the South China Sea: Climatological mean and annual variability, *Atmos. Oceanic Sci. Lett.*, *5*, 15–19.
Yuan, D., W. Han, and D. Hu (2006), Surface Kuroshio path in the Luzon Strait area derived from satellite remote sensing data, *J. Geophys. Res.*, *111*, C11007, doi:10.1029/2005JC003412.
Yuan, Y., Y.-H. Tseng, C. Yang, G. Liao, C. H. Chow, Z. Liu, X.-H. Zhu, and H. Chen (2014), Variation in the Kuroshio intrusion: Modeling and interpretation of observations collected around the Luzon Strait from July 2009 to March 2011, *J. Geophys. Res.*, *119*, 3447–3463, doi:10.1002/2013JC009776.
Zhang, H.-M., J. J. Bates, and R. W. Reynolds (2006), Assessment of composite global sampling: Sea surface wind speed, *Geophys. Res. Lett.*, *33*, L17714, doi:10.1029/2006GL027086.
Zhang, W.-Z., F. Shi, H.-S. Hong, S.-P. Shang, and J. T. Kirby (2010), Tide-surge interaction intensified by the Taiwan Strait, *J. Geophys. Res.*, *115*, C06012, doi:10.1029/2009JC005762.
Zhang, W.-Z., F. Chai , H.-S. Hong, and H. Xue (2014), Volume transport through the Taiwan Strait and the effect of synoptic events, *Cont. Shelf Res.*, *88*, 117–125, doi:10.1016/j.csr.2014.07.010.
Zhang, W.-Z., H. Xue, F. Chai, and Q. Ni (2015a), Dynamical processes within an anticyclonic eddy revealed from Argo floats, *Geophys. Res. Lett.*, *42*, 2342–2350, doi:10.1002/2015GL063120.
Zhang, W.-Z., X.-F. Zhuang, C. T. A. Chen, and T.-H. Huang (2015b), The impact of Kuroshio water on the source water of the southeastern Taiwan Strait: Numerical results, *Acta Oceanol. Sin.*, *34*(9), 23–24, doi:10.1007/s13131-015-0720-x.
Zhang Y., D. Wang, H. Xia, and L. Zeng (2012), The seasonal variability of an air-sea heat flux in the northern South China Sea, *Acta Oceanol. Sin.*, *31*, 79–86.